Study of conduction welded C-struts for a thermoplastic composite fuselage

Paz Méndez, Javier; Raimondo, Antonio; Bisagni, Chiara

DOI
10.1080/15376494.2024.2344028

Publication date
2024

Document Version
Final published version

Published in
Mechanics of Advanced Materials and Structures

Citation (APA)
Paz Méndez, J., Raimondo, A., & Bisagni, C. (2024). Study of conduction welded C-struts for a thermoplastic composite fuselage. *Mechanics of Advanced Materials and Structures*, *32*(3), 246-259. https://doi.org/10.1080/15376494.2024.2344028

Mechanics of Advanced Materials and Structures

ISSN: (Print) (Online) Journal homepage: www.tandfonline.com/journals/umcm20

Study of conduction welded C-struts for a thermoplastic composite fuselage

Javier Paz Méndez, Antonio Raimondo & Chiara Bisagni

To cite this article: Javier Paz Méndez, Antonio Raimondo & Chiara Bisagni (24 Apr 2024): Study of conduction welded C-struts for a thermoplastic composite fuselage, Mechanics of Advanced Materials and Structures, DOI: 10.1080/15376494.2024.2344028

To link to this article: https://doi.org/10.1080/15376494.2024.2344028

MECHANICS OF ADVANCED MATERIALS AND STRUCTURES
https://doi.org/10.1080/15376494.2024.2344028

ORIGINAL ARTICLE

Study of conduction welded C-struts for a thermoplastic composite fuselage

Javier Paz Méndez[a,b], Antonio Raimondo[a,c], and Chiara Bisagni[a,d]

[a]Faculty of Aerospace Engineering, Delft University of Technology, Delft, The Netherlands; [b]Aerospace Systems and Transport Research Group, Universidad Rey Juan Carlos, Madrid, Spain; [c]Department of Aerospace Engineering, Universidad Carlos III de Madrid, Madrid, Spain; [d]Department of Aerospace Science and Technology, Politecnico di Milano, Milano, Italy

ABSTRACT
In this research, conduction welded C-struts, part of a thermoplastic composite fuselage designed and manufactured in the framework of the Clean Sky 2 STUNNING project, are investigated. Five specimens made of two C-section profiles are manufactured and welded using conduction welding in three different configurations with variations in the direction and distance of the two welded joints. Preliminary numerical analysis using the virtual crack closure technique are conducted to obtain an initial evaluation of the specimens behavior, in preparation of the tests. Experiments are performed under quasi-static loading conditions to measure the strength of the welds. Comparisons with the preliminary numerical analyses show a good agreement in terms of the predicted maximum load, while a clear difference is observed in the initial stiffness, due to the compliance of the support structure. The numerical model is updated, leading to results that closely match the experimental behavior. For all the analyzed specimens, the separation occurs suddenly and no signs of propagation are observed. Experimental and numerical data show no relevant difference in the joint strength among the different conduction welding configurations.

ARTICLE HISTORY
Received 8 April 2024
Accepted 12 April 2024

KEYWORDS
Thermoplastic composite; conduction welding; experimental test; numerical analysis; virtual crack closure technique

1. Introduction

In aeronautics, it is more and more important to explore novel design approaches and materials that can allow significant advances toward achieving the targets of increased sustainability. One major breakthrough for efficiently addressing this competing need dwells in the use of thermoplastic composites, made from a thermoplastic matrix reinforced with fibers [1, 2]. Compared to traditional thermoset, thermoplastic composites exhibit higher fracture toughness [3], have the ability to undergo multiple melting cycles while maintaining their mechanical characteristics rendering them highly sustainable for recycling [4], and their reversibility enables the reprocessing and repair of parts [5]. Furthermore, there has been a recent surge of interest among researchers in fabricating these materials using additive manufacturing technologies [6].

The re-melting capabilities of the thermoplastic matrix allow for expanded manufacturing and joining possibilities, such as thermoplastic welding [7–9]. In thermoplastic welding, two parts are joined by applying heat and pressure to locally melt the material, which results in much shorter processing times when compared to other manufacturing techniques as autoclave-, oven- and press-consolidation. The most common thermoplastic welding techniques are resistance, induction, and ultrasonic welding [10–12]. However, another method has arisen in the form of conduction welding, which is based on using an induction-heated tool to heat the surface of the part and creating the weld bath through heat conduction within the laminate. This method has been developed at GKN Fokker [13, 14] and provides benefits as it does not require addition of welding specific materials, such as energy directors or conductive strips, resulting more suitable and scalable for welding of large parts, and offering a higher robustness against manufacturing tolerances like gaps.

In the European project Clean Sky 2, “SmarT mUltifuNctioNal and INtegrated TP fuselaGe” STUNNING, the development of thermoplastic composites for aircraft primary structures was explored through the manufacturing of the lower half of a thermoplastic fuselage demonstrator [15]. The objective was to validate the effectiveness of combining different structural elements and components using advanced materials and cutting-edge joining techniques for the next-generation aircraft [16]. In this context, different welding and joining methods were used to assemble the demonstrator, taking into account industrial scalability and seamless integration with other production process.

The use of fastener-free connection poses significant challenges. Accurately forecasting the strength of welded joints requires the need for a comprehensive investigation to ensure reliable performance in structural applications [17, 18].

The influence of composite lay-up and R-curve on the mechanical strength of thermoplastic single lap joints have been experimentally and numerically investigated in [19, 20]. In [21], researchers evaluated the failure behavior of composite thermoplastic stiffened panels in post-buckling conditions, revealing a distinct structural response compared

CONTACT Chiara Bisagni chiara.bisagni@polimi.it Department of Aerospace Science and Technology, Politecnico di Milano, Milano, Italy.

to thermoset stiffened panels, with a combination of stable and unstable crack growth. The effect of temperature on the mechanical characteristics of thermoplastic composites has been explored in [22], demonstrating significant variations in the compression and flexural properties with temperature changes. Furthermore, in [23, 24] the energy-absorption and dynamic response of thermoplastic materials have been assessed, indicating improvements in both viscous responses and energy dissipation.

Different approaches have been employed in literature to predict the strength of thermoplastic welded joints using finite elements [25, 26]. The Cohesive Zone Model (CZM) has been successfully adopted in [27] to evaluate the failure behavior and to characterize the crack propagation of conduction welded joints in single lap shear specimens. However, the numerical cost of employing the CZM is high, as it requires small element sizes in the process zone to accurately analyze crack propagation, limiting its applicability to small specimens. On the other hand, within the STUNNING project, the Virtual Crack Closure Technique (VCCT) approach has been proved to be effective in investigating the strength of welded joints in larger components. In [28], the VCCT has been adopted to analyze the structural performance and the failure load of thermoplastic composite stiffened panels in post-buckling loading conditions where the skin and the stringer were joined using conduction welding.

The majority of research on thermoplastic welding available in the literature has been conducted on small coupons, with limited experimental and numerical data available on elements or sub-components. In this paper, conduction welded specimens used in the STUNNING fuselage are studied to characterize the strength and failure behavior.

The objective is to investigate the conduction welding strength of a critical component in the lower fuselage section, the vertical strut, which connects the fuselage frame with the horizontal floor structure. Quasi-static experimental tests are performed and Digital Image Correlation (DIC) is employed to capture the deformation field during the load application. The structural behavior is analyzed using finite element analysis where the welding separation is modeled using the VCCT approach. In Section 2, the specimens are described in terms of geometry, material and different

Table 1. LM-PAEK Toray Cetex TC1225 elastic material properties [30].

E_1 [GPa]	$E_2 = E_3$ [GPa]	$G_{12} = G_{13}$ [GPa]	G_{23} [GPa]	$\nu_{12} = \nu_{13}$ [-]	ρ [kg/m^3]
110.00	9.00	4.30	3.00	0.363	1540.0

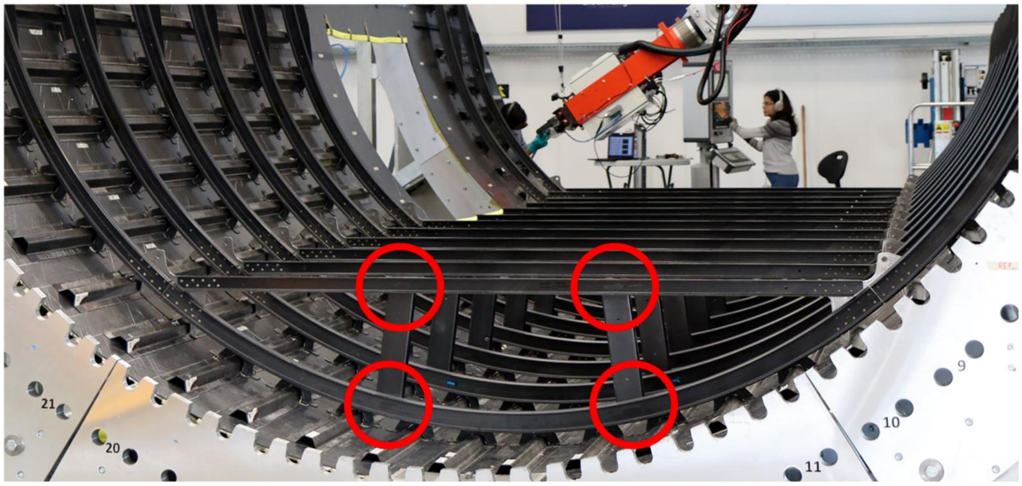

Figure 1. Lower section of the STUNNING fuselage. Adapted from [29].

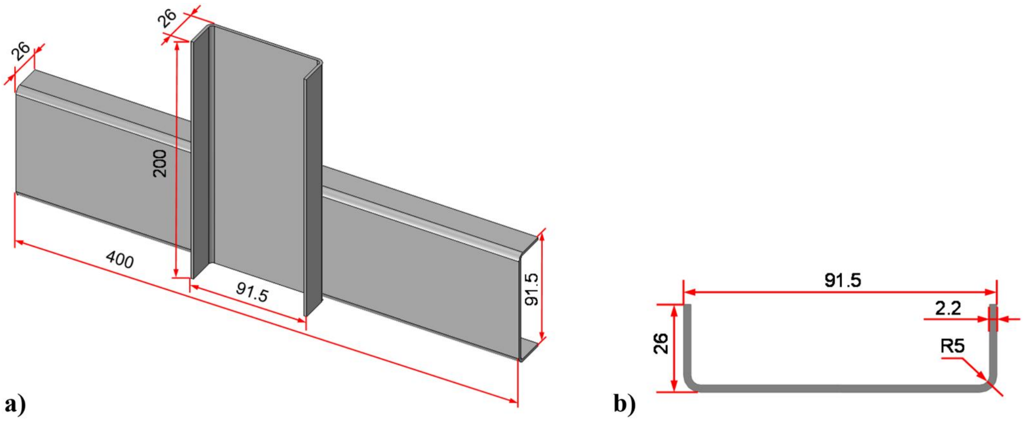

Figure 2. Specimen dimensions: (a) isometric view; (b) cross-section of C-profile (dimensions in mm).

Figure 3. Test specimens.

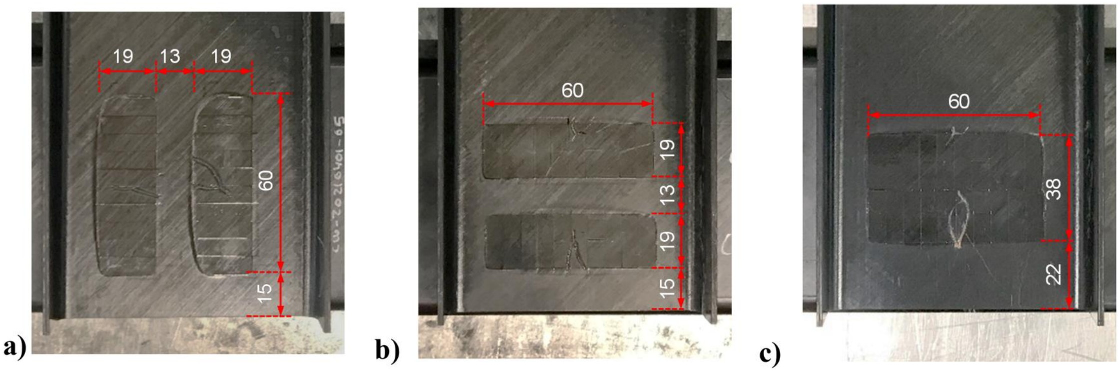

Figure 4. Geometry and nominal dimensions of the welded strips for the three configurations: (a) vertical; (b) horizontal; (c) horizontal (joined) (dimensions in mm).

Table 2. Specimen characteristics: weight and average measurements.

Specimen	Welding configuration	Weight [g]	Average thickness [mm]	Distance between welds [mm]
1	Vertical	276.3	2.17	13.0
2	Vertical	277.6	2.22	13.6
3	Horizontal	277.9	2.18	12.6
4	Horizontal	276.8	2.20	12.5
5	Horizontal (joined)	277.1	2.20	0.0

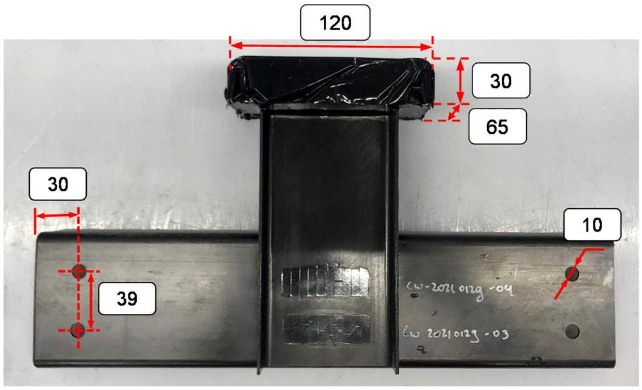

Figure 5. Test specimen with resin tab and holes for attachment to support structure (dimensions in mm).

welding characteristics. Section 3 presents the results of preliminary numerical analyses performed in preparation of the experimental tests. In Section 4, the test set-up is described and the experimental results are presented for each welding configuration, in terms of load-displacement curves and DIC images, and are compared with the preliminary numerical outcomes. Finally, in Section 5, the numerical model is updated and validated using the experimental data.

Table 3. Properties of casting Resin RenCast® CW 2418-1 hardened with ren® HY 5160-1 [31].

E [GPa]	ν [–]	ρ [kg/m^3]
5.0	0.3	2300

2. Welded C-struts

The specimens investigated in this study consist of two C-section profiles, identical in term of geometry, material and welding process to the profile used in the STUNNING fuselage demonstrator. Figure 1 shows the lower half of this fuselage demonstrator, where the main structural features, as

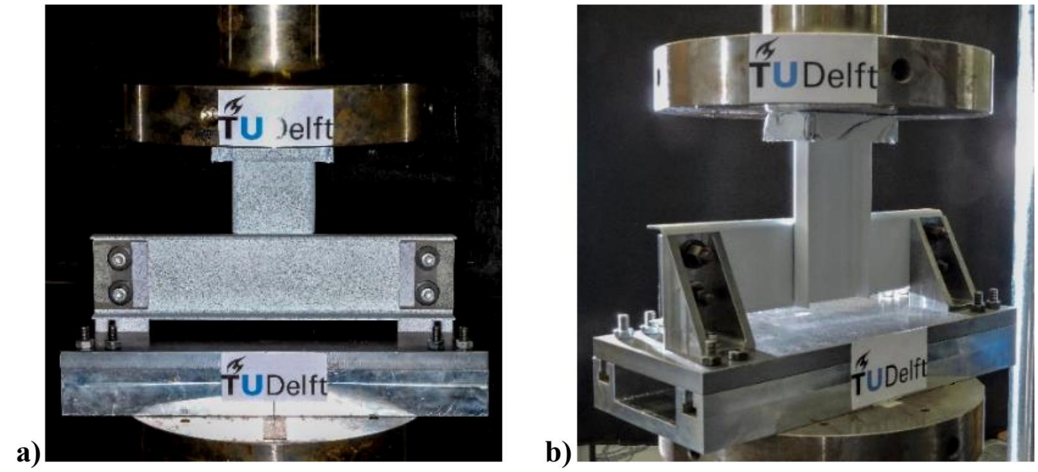

Figure 6. Test specimen and support structure: (a) front view; (b) rear view.

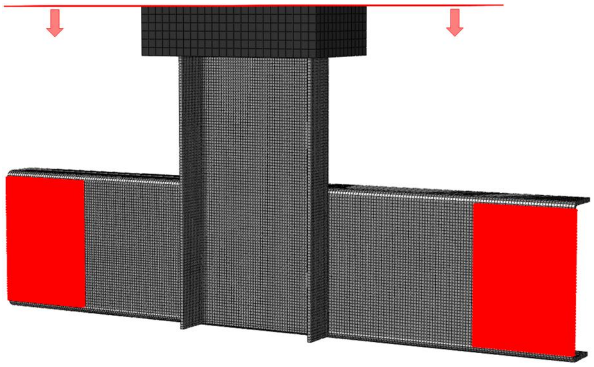

Figure 7. FE model with applied boundary conditions.

Table 4. LM-PAEK Toray Cetex TC1225 interface material properties [30].

G_{Ic} [N/m]	G_{IIc}=G_{IIIc} [N/m]	η [–]
969.0	1719.0	2.284

the omega-stiffened skin, frames, vertical struts, and cargo beams can be seen. The areas highlighted in red indicate the regions objective of this study. The behavior of these joints is critical to the overall aircraft performance, both in terms of strength under normal operation conditions as well as in the event of a crash.

The specimens are made by joining perpendicularly, through conduction welding, two C-section profiles in a T shape, as shown in Figure 2a. The horizontal and vertical profiles have an identical cross-section, with dimensions specified in Figure 2b, and different lengths, 200 and 400 mm, respectively. The components consist of 12 unidirectional plies with a nominal ply thickness of 0.184 mm of T700/LM-PAEK Toray 194 gsm thermoplastic composite with layup [45/−45/0/0/90/45/−45/90/0/0/−45/45], yielding a nominal total laminate thickness of 2.208 mm. The material properties of the T700/LM-PAEK thermoplastic composite are taken from [30] and are reported in Table 1.

Five specimens were manufactured and welded by GKN Fokker, attaching one end of the short profile to the web of the 400 mm profile at its center. A photo of the five specimens is reported in Figure 3.

The conduction welding process developed by GKN Fokker [13, 14] operates by locally heating the surface of the part, producing the weld bath via heat conduction. Pressure is applied simultaneously with heating, with the opposing anvil reacting to this force. Both stamps and heatsinks constitute the weld tooling, designed to adapt to changes in laminate thickness along the welding direction. The main advantages of this process are that it can be scaled up to large aerospace components and does not require the use of additional welding-specific materials, like energy directors or conductive strips. However, the technology at the time of this research was limited to a weld interface width of approximately 20 mm. For this reason, welding of wider areas had to be performed using multiple strips. In this work, the five specimens were joined using three different welding configurations, with variations in the direction of the welds and in the distance between the two weld strips. Each weld strip is 60 mm long and 19 mm wide, and the two strips are placed so that the center of the combined welded area is at the center of the contact region between both profiles. An example of each welding configuration is shown in Figure 4. Figure 4a shows the configuration referred to as “Vertical”, with the strips placed vertically at a nominal distance of 13 mm, used for specimens 1 and 2. The configuration named “Horizontal” can be seen in Figure 4b, where the weld strips are rotated 90 degrees respect to the previous configuration, but still spaced 13 mm apart. This configuration is used for specimens 3 and 4. The third configuration, shown in Figure 4c, is the “Horizontal (joined)” with the weld strips placed horizontally but without any separation between them. This configuration is used for specimen 5.

The specimen number and welding configuration are presented in Table 2, together with the weight, the average thickness and the distance measured between the weld strips. The average thickness is calculated by taking six measurements per profile at different locations. Values show a good consistency between all specimens with a maximum deviation from the nominal values of 1.4% for the thickness and 4.6% for the distance between welds.

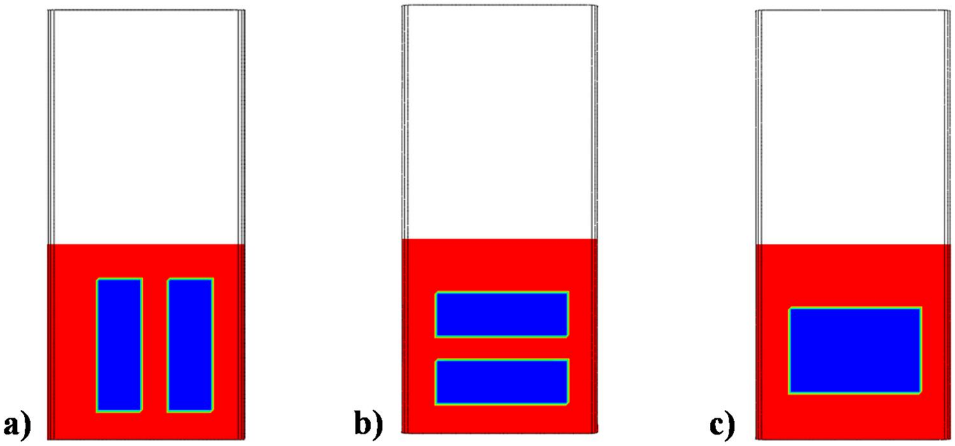

Figure 8. Position of the welding in the numerical model for the three configurations: (a) vertical; (b) horizontal; (c) horizontal (joined).

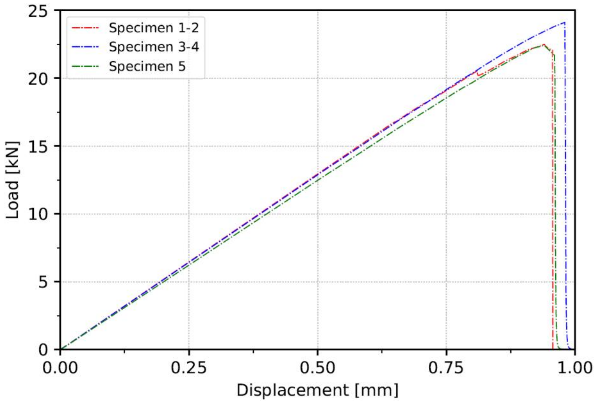

Figure 9. Load-displacement curves obtained from the preliminary analyses for the three welding configurations.

To ensure a uniform application of the load and reduce stress concentrations at the profile upper edge during the tests, the last 30 mm of the shorter C-profile are embedded in a tab of metal-filled casting resin RenCast® CW 2418-1 hardened with Ren® HY 5160-1, as shown in Figure 5. The outermost face from the tab is then machined to ensure that the axial load is evenly distributed along the edge. The resin density and elastic properties are taken from the manufacturer material datasheet [31] and are reported in Table 3.

Four holes are then drilled to the long C-profile, two at each end, so that the specimens can be attached to the support structure during testing. The centers of the holes are 39 mm apart and 30 mm from the edge, as shown in Figure 5.

The components are then painted and speckled for the digital image correlation (DIC), as shown in Figure 6. First, three layers of matte white paint are sprayed over the components to provide a homogeneous background color. Then, the specimens are painted with black speckles, approximately 1 mm in diameter providing around 40% of coverage over the white base.

A support structure, shown in Figure 6, is used to constrain the movement and rotation of the ends of the horizontal beam so to reproduce the behavior of the remaining part of the passenger floor during the application of the vertical load. The support structure consists of a steel flat plate of 500 × 150 mm with a thickness of 10 mm, used as a base, to which two mounting brackets of 60 × 90 mm are attached.

3. Preliminary analysis

Before performing the tests, preliminary Finite Element (FE) analyses are conducted to obtain an initial evaluation of the stiffness, maximum loads and maximum displacements as prediction of the experimental results. In this section, the FE model developed for the preliminary analysis is described and the numerical results are compared among the three different welding configurations.

3.1. Finite element models

The pretest numerical models are developed using the Abaqus 2021 software [32]. Three different models are considered to account for the three different welding configurations: Vertical, Horizontal, and Horizontal (joined). The discretization of the two C-profiles is done using 8-node continuum shell elements with reduced integration and hourglass control (SC8R). An element size of 1.75 mm is selected after performing a mesh sensitivity analysis, resulting in a total of 27,405 elements and 55,820 degrees of freedom. Particular care is taken to have regular coincident nodes where the C-profiles overlap. For the resin tab, 1872 8-node hexahedral 3D elements (C3D8R) with an average size of 5 mm are used; whereas the loading plate at the top is modeled as an analytical rigid. The FE model of the specimen is shown in Figure 7.

Boundary conditions are applied to the end regions of the horizontal C-profile of the specimen, highlighted in red in Figure 7, where all degrees of freedom are fixed to mimic the effect of the support structure used in the tests. The load is introduced by vertically displacing the loading plate following the arrow directions in Figure 7 and fixing all other degrees of freedom. The contact properties between the loading plate and the specimen resin tab are set to hard contact for the normal direction, and with a friction coefficient of 0.2 for the tangential direction.

Table 5. Results from the preliminary numerical analyses for the three welding configurations.

Specimen	Welding configuration	Initial stiffness [kN/mm]	Welding separation load [kN]	Maximum load [kN]	Displacement at maximum load [mm]
1-2	Vertical	25.9	12.9	22.5	0.95
3-4	Horizontal	25.9	13.9	24.1	0.98
5	Horizontal (joined)	25.0	13.5	22.4	0.96

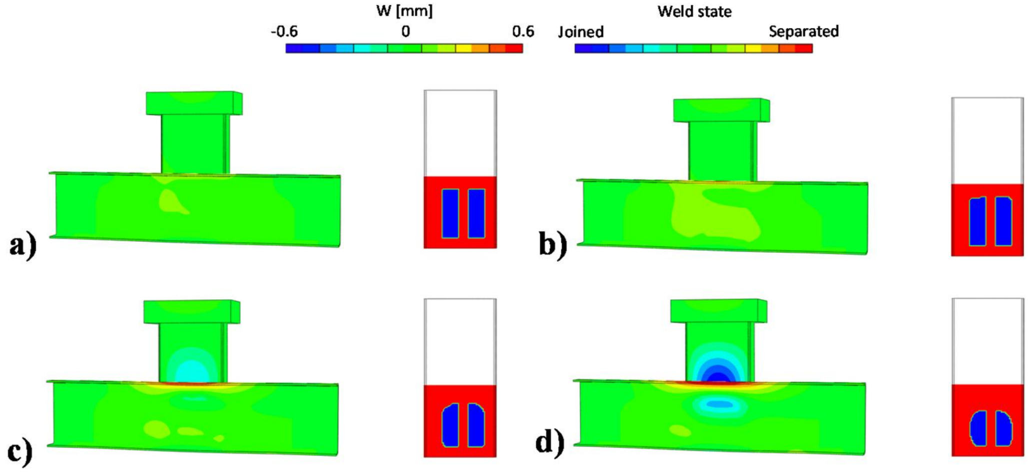

Figure 10. Out-of-plane displacements and weld state of the "vertical" configuration at: (a) F = 12.2 kN – d = 0.45 mm; (b) F = 17.1 kN – d = 0.65 mm; (c) F = 21.0 kN – d = 0.85 mm; (d) F = 22.5 kN – d = 0.94 mm.

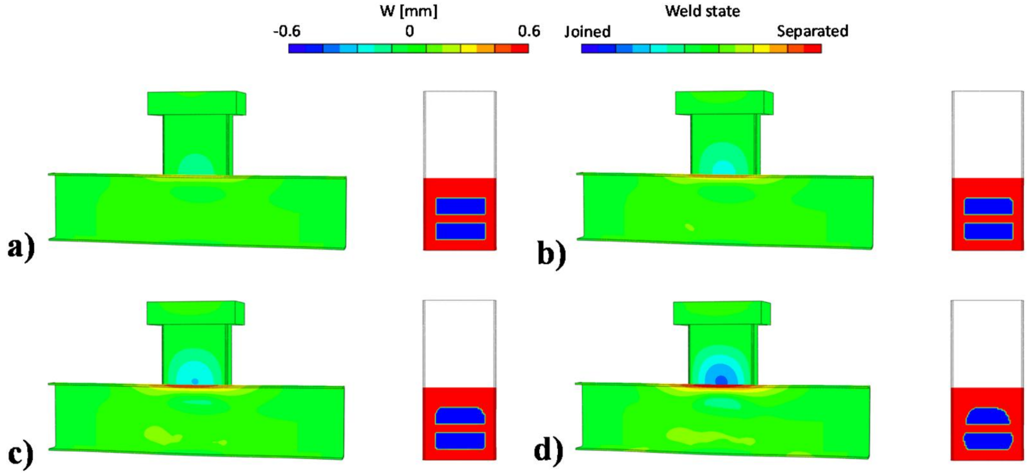

Figure 11. Out-of-plane displacements and weld state of the "horizontal" configuration at: (a) F = 12.4 kN – d = 0.48 mm; (b) F = 17.4 kN – d = 0.68 mm; (c) F = 20.9 kN – d = 0.82 mm; (d) F = 24.1 kN – d = 0.98 mm.

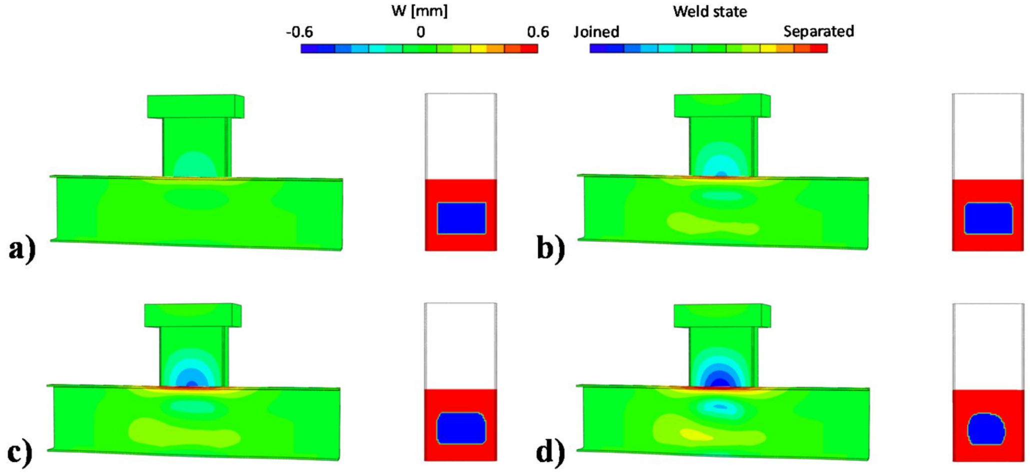

Figure 12. Out-of-plane displacements and weld state of the "horizontal (joined)" configuration at: (a) F = 12.0 kN – d = 0.48 mm; (b) F = 17.3 kN – d = 0.70 mm; (c) F = 20.6 kN – d = 0.84 mm; (d) F = 22.4 kN – d = 0.95 mm.

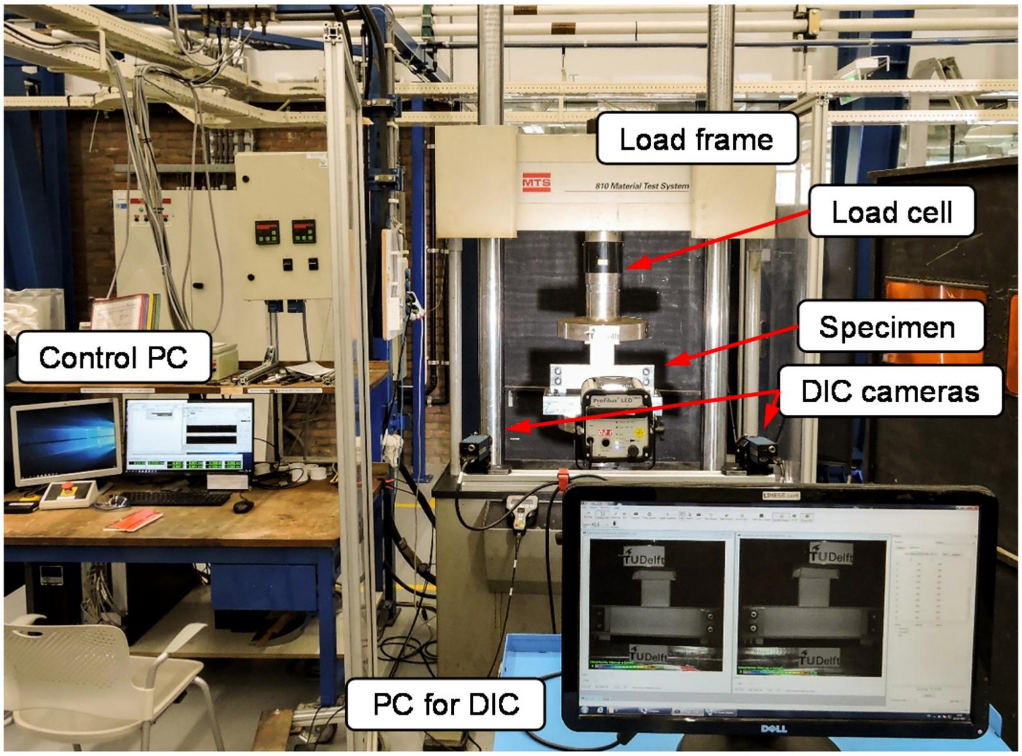

Figure 13. Test set-up and instrumentation.

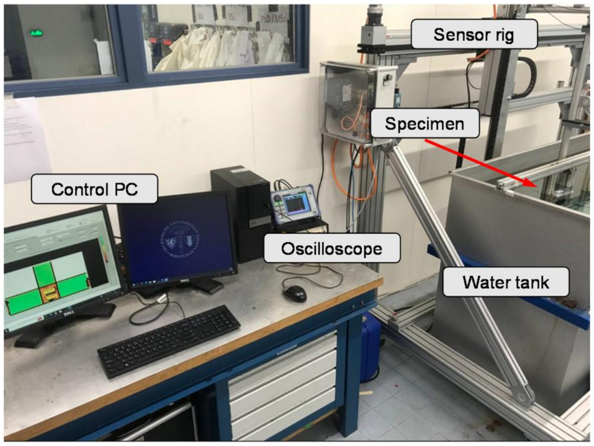

Figure 14. Ultrasonic C-scan system.

The interlaminar behavior of the welding is simulated using the virtual crack-closure technique (VCCT), implemented within the FE code Abaqus. The nodes of the two surfaces in contact in the welded regions are initially tied. Their connection is released when the energy release rate is higher than the critical fracture toughness, evaluated according to the criterion proposed by Benzeggangh and Kenane [33], reported in Eq. (1).

$$G_c = G_{Ic} + (G_{IIc} - G_{Ic})\left(\frac{G_{II} + G_{III}}{G_I + G_{II} + G_{III}}\right)^{\eta} \qquad (1)$$

The used interface material properties are reported in Table 4. It is assumed that the mode III fracture toughness is equal to the mode II fracture toughness.

The size and location of the welding strips are taken from Figure 4. Each welding strip is assumed to be a rectangle 60 mm in length and 19 mm in width. The position of the welded strips in the numerical model is displayed in Figure 8, where the areas in blue are the regions where the coincident nodes of the horizontal and vertical profile are initially connected to represent the welding interface.

Quasi-static analyses are performed under displacement-controlled conditions, to predict the structural behavior of the experimental tests, using the dynamic implicit solver to regularize the unstable behavior of the model and improve the convergence rate during the failure of the welding.

3.2. Preliminary numerical results

The load-displacement curves resulting from the pretest numerical analyses are reported in Figure 9, with a summary of the most relevant obtained values presented in Table 5. The table reports the initial stiffness evaluated between 5 and 10 kN, the load when the welding separation initiates, the maximum load and the corresponding displacement. It can be seen that the differences in the behavior of the components are minor among the different configurations. The specimen with the two horizontal weld strips, specimens 3 and 4, outperforms the other two configurations showing the highest welding separation load and withstand a maximum load around 7.5% higher. Specimen 5, with the horizontal joined weld strips, shows a stiffness value approximately 3.5% lower than the other welding configurations.

Figures 10–12 report the out-of-plane displacements and the state of the welded regions for specimens 1–2, 3–4 and 5, respectively. Regarding the direction of the out-of-plane

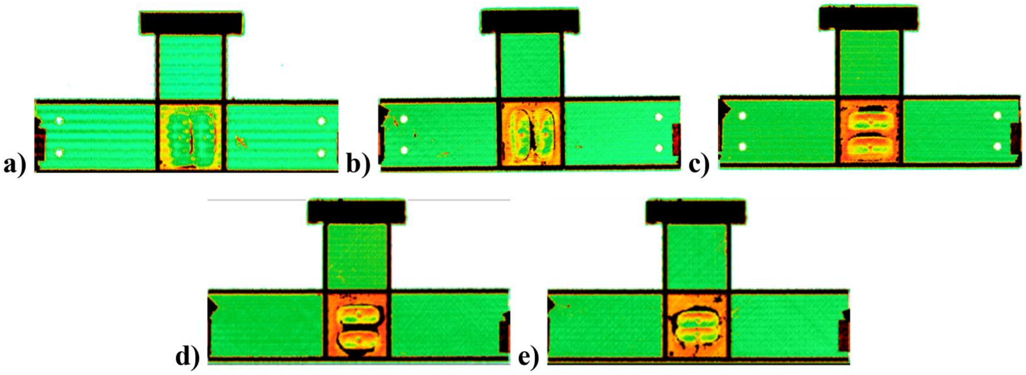

Figure 15. Ultrasonic C-scans of specimens before testing: (a) specimen 1; (b) specimen 2; (c) specimen 3; (d) specimen 4; (e) specimen 5.

Table 6. Results from the tests.

Specimen	Welding configuration	Initial stiffness [kN/mm]	Maximum load [kN]	Displacement at maximum load [mm]
1	Vertical	16.75	23.4	1.72
2	Vertical	16.62	22.8	1.62
3	Horizontal	17.25	22.5	1.60
4	Horizontal	17.01	23.7	1.69
5	Horizontal (joined)	17.25	24.5	1.70

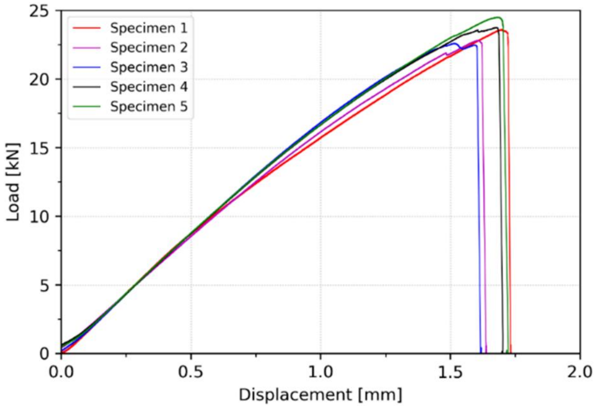

Figure 16. Load-displacement curves from the tests.

displacements, positive values correspond to displacements toward the viewer. The regions fully welded correspond to the blue color, while separated regions are represented in red.

A common behavior is noticed among all specimens, in which the separation of the welded regions begins in the upper part of the weld (seen in Figures 10b, 11b, and 12b). This may be caused by the small out-of-plane displacement of the upper flange of the horizontal profiles, which introduces mode I interface stresses in the weld. As the load increases, the lower flange of the horizontal profile also begins to separate from the vertical profile, although not so much as the upper flange. This in turn fosters that the lower corners of the welds also begin to separate (Figures 10c, 11c, and 12c). Figures 10d, 11d, and 12d report the status before the complete separation of the two parts.

4. Experimental tests

In this section, an overview of the test set-up adopted in the experimental campaign is illustrated. Then, the experimental results are presented and compared with the results of the preliminary numerical analysis.

4.1. Test set-up

The tests are performed under displacement-controlled conditions in the MTS 810 Material Testing System shown in Figure 13, with the upper machine plate fixed and the bottom plate moving upwards at a loading rate of 0.1 mm/min. The servo-hydraulic testing machine is equipped with a displacement sensor and a 500 kN load cell, which provides displacement and load data during the tests. A PC is used to control the testing machine and manage data acquisition, another PC is used to control the DIC equipment, and a laptop is used to record test logs and partially post-process data during the tests. Before the tests, the specimens are measured to determine the center of mass from the encased cross-section disregarding the resin tabs, so to align the center of mass with the center of the loading plates to reduce any non-axial loads on the component.

For all the tests one three dimensional DIC system (VIC3D [34]) is used to measure the in-plane and out-of-plane displacements capturing images every 3 s.

An ultrasonic through-transmission C-scan system, shown in Figure 14, is used before the tests to detect any manufacturing defects and to assess the extension of the weld in each specimen.

The system consists of a 5 MHz Olympus OmniScan SX ultrasonic emitter and a receiver. The specimens are placed in a water basin between the emitter and the receiver so that the signal dampened by the component can be measured. This allows to detect possible delamination or areas which are not properly welded. The pretest C-scans of all five specimens are shown in Figure 15, where the colors represent the percentage of the ultrasound waves damping. The areas in green are representative of regions where there is

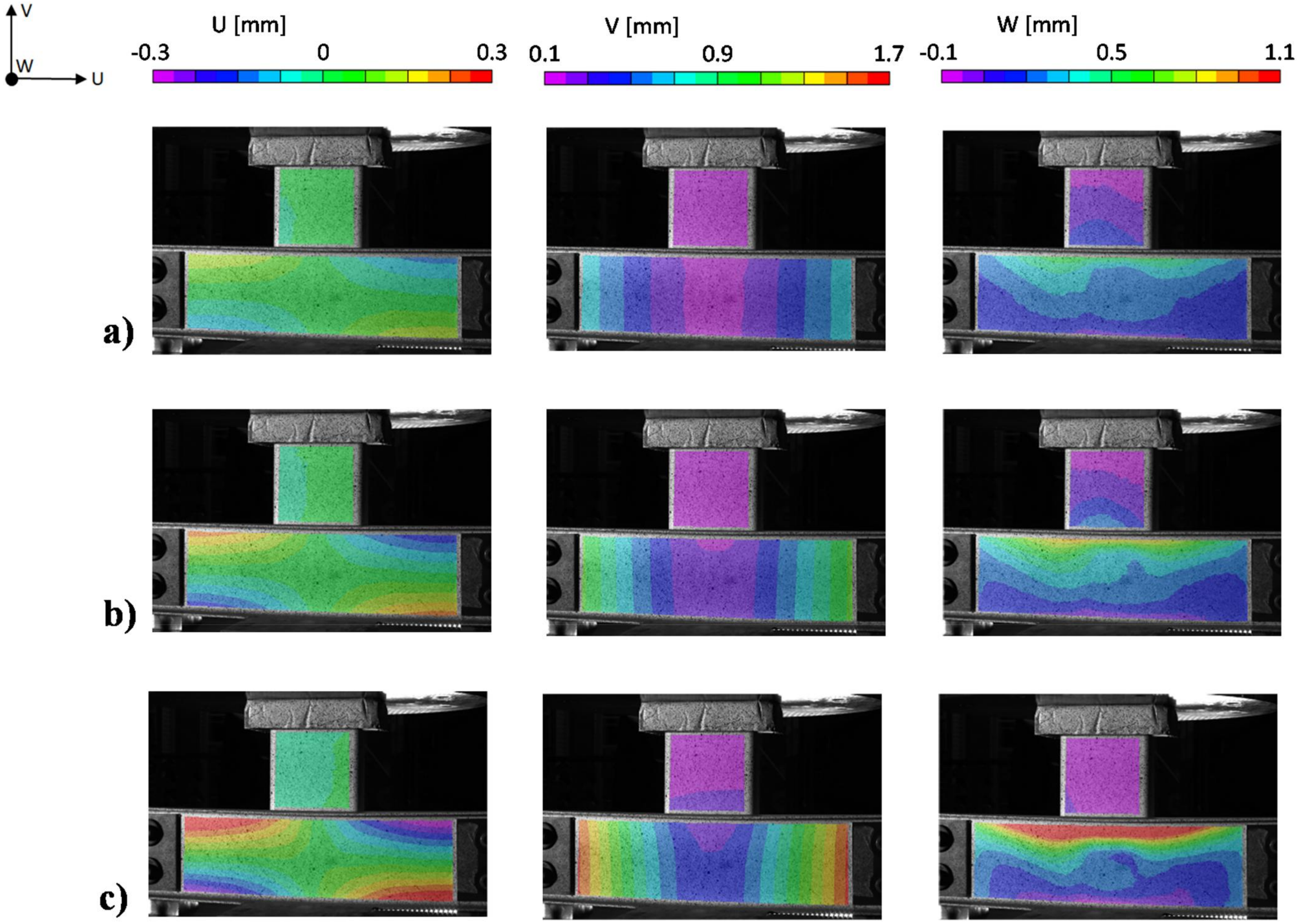

Figure 17. Displacement components measured on specimen 1 (vertical welding configuration) at: (a) F = 12.2 kN – d = 0.75 mm; (b) F = 17.1 kN – d = 1.10 mm; (c) F = 22.9 kN – d = 1.72 mm.

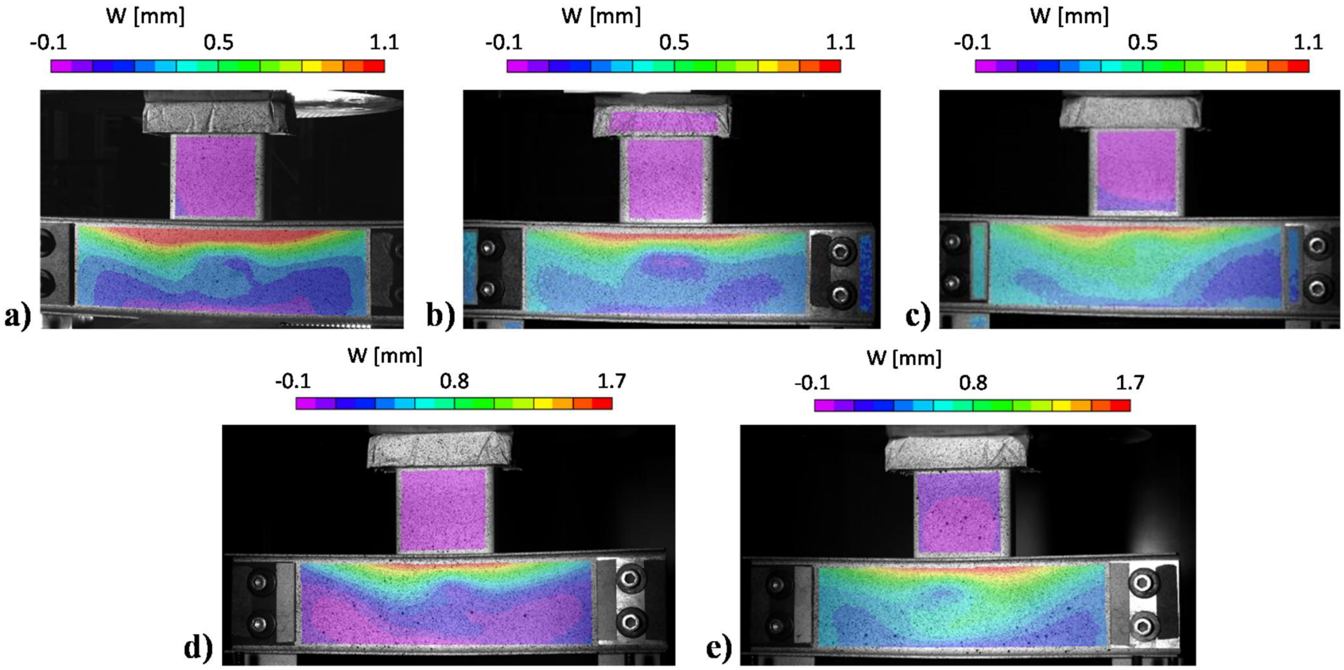

Figure 18. Out-of-plane displacement measured at the maximum load: (a) specimen 1; (b) specimen 2; (c) specimen 3; (d) specimen 4; (e) specimen 5.

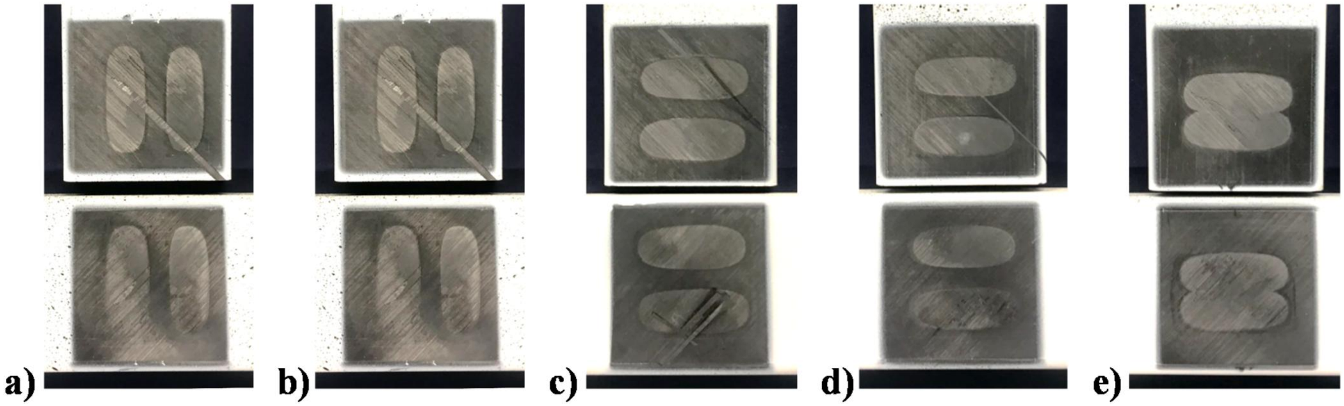

Figure 19. Welded interface after separation: (a) specimen 1; (b) specimen 2; (c) specimen 3; (d) specimen 4; (e) specimen 5.

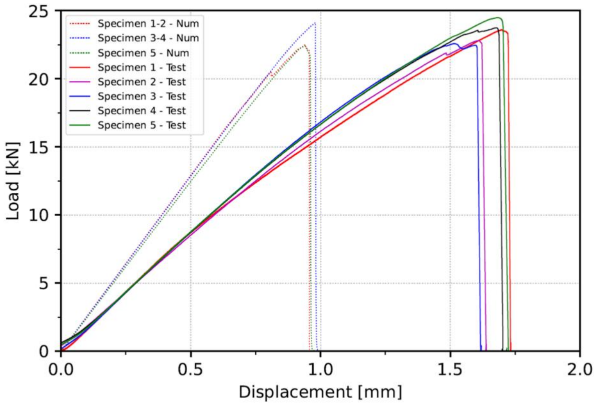

Figure 20. Preliminary numerical and experimental load-displacement curves for the three welding configurations.

limited or no attenuation, indicating the absence of discontinuities through the thickness. In the areas in orange and red, where the overlap of both profiles occurs in the not welded regions, the signal damping is maximum indicating the unconnected areas. The welded regions can be easily identified within the overlap area, as the welded zones promote a better signal propagation thus yielding a color between green and orange.

4.2. Experimental results

A summary of the data obtained from the tests of the five specimens is reported in Table 6. Since the use of the DIC software allows to accurately characterize the actual displacements of the specimen without the compliance of the machine or of the supporting structure, load-displacement curves are evaluated in which the displacement is taken from the DIC measurements while the force is retrieved from the machine load cell. The resulting curves are reported in Figure 16.

Although some scatter can be noted, the differences are small. In the case of the initial stiffness, values fluctuate around 4%, ranging between 16.62 kN/mm for specimen 2 and 17.25 kN/mm for specimens 3 and 5. It can also be seen that the specimens with the vertical welding, specimens 1 and 2, exhibit stiffness values that are on average 3% lower than those with the horizontal welds. This difference is more visible in the curves in the range between 10 kN and 20 kN. Regarding the maximum loads, they range between 22.5 kN for specimen 3, and 24.5 kN for specimen 5 with a difference of about 8%. As already noted from the results of the preliminary numerical analyses, no relevant differences can be observed between the analyzed welding configurations in terms of maximum force and displacement. For all specimens, the separation occurs suddenly and no signs of propagation are observed, except for small drops in the load-displacement curves for specimens 2, 3 and 4, right before the collapse.

Figure 17 offers the in-plane (U, V) and out-of-plane (W) displacements of specimen 1 measured using DIC at different loads. The progression of the in-plane horizontal displacements (U, positive values indicate displacement to the right), shown in the first column of Figure 17, reveals how the four corners of the horizontal C-section move slightly due to the bending of the support structure, with a maximum displacement of 0.3 mm (Figure 17c).

The in-plane vertical displacements (V, positive values indicate displacement upwards) are shown in the second column of Figure 17. It can be seen how the upper part of the specimen stays fixed, while the sides where the specimen is bolted to the support progressively move upwards. The symmetry between the displacements at both sides of the support structure demonstrates that the specimen is uniformly loaded, successfully constraining any rotation of the lower C-profile. The maximum displacement of the specimen is around 1.7 mm (Figure 17c), approximately 0.5 mm lower than the value measured from the machine data, which can be partially attributed to the compliance of the testing machine.

The out-of-plane displacements (W, positive values indicate displacement toward the viewer) are shown in the third column of Figure 17. It can be noted that the upper flange of the horizontal C-profile progressively moves toward the viewer, and the maximum out-of-plane displacement recorded by the DIC system is 1.1 mm.

Despite the different welding configurations, the in-plane behavior of all five specimens is similar, both qualitatively and quantitatively. However, there are slight differences in the out-of-plane behavior, as can be seen in Figure 18, where the distribution of the out-of-plane displacements is

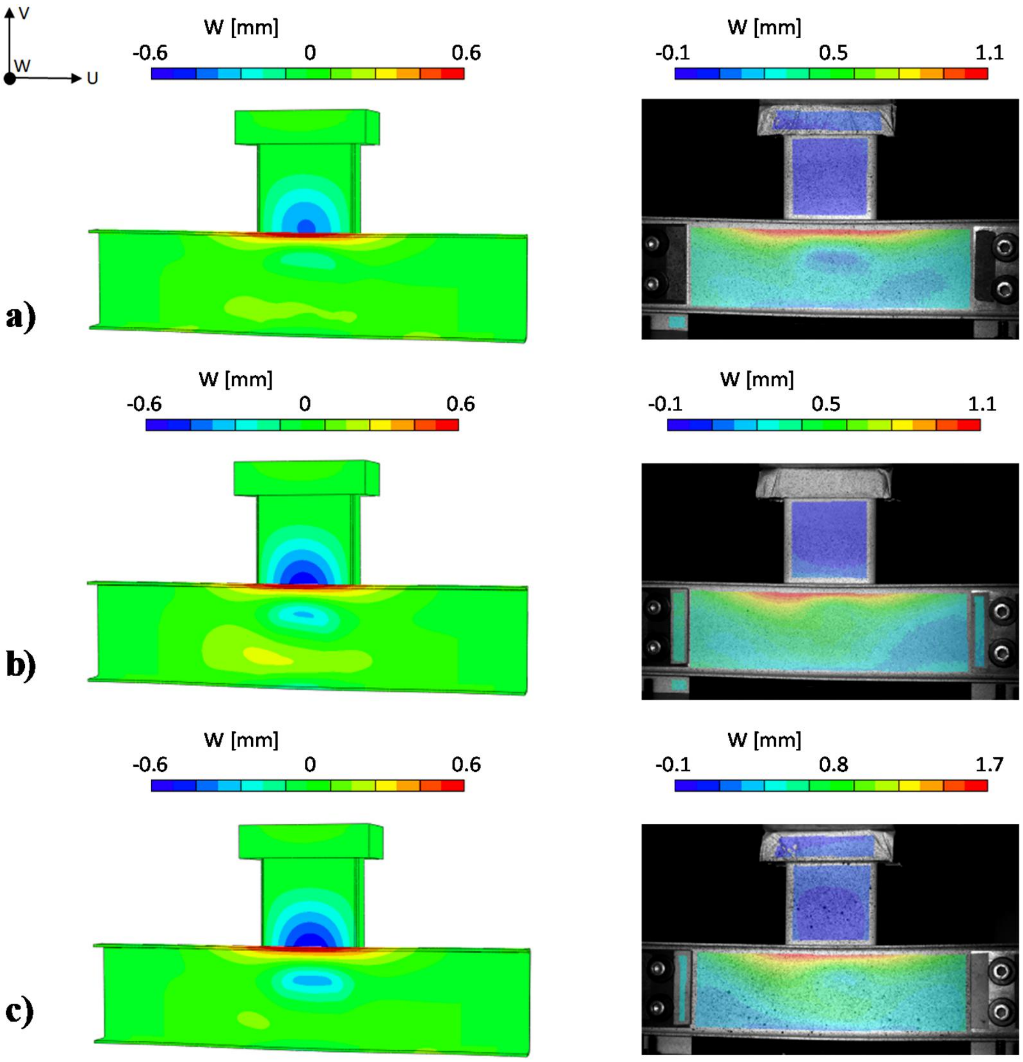

Figure 21. Comparison of out-of-plane displacements between numerical simulation and test before the complete separation: (a) specimen 2; (b) specimen 3; (c) specimen 5.

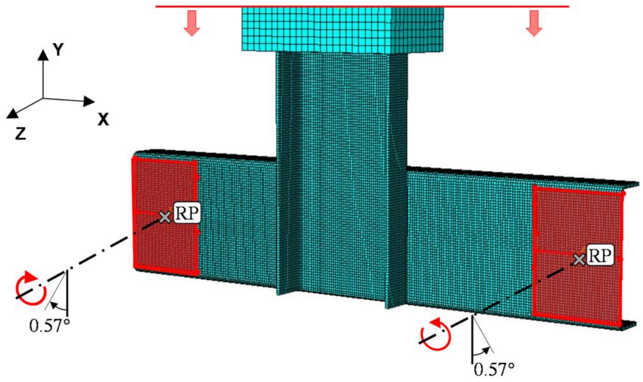

Figure 22. Boundary conditions of the updated FE model.

shown for the five specimens just before the complete separation of the welded regions.

While for all the specimens the lower part of the horizontal C-profile moves slightly toward the viewer, between 0.4 and 0.5 mm, for specimen 1 (Figure 18a) and specimen 4 (Figure 18d) the same region displaces away from the viewer of approximately 0.1 mm.

The welded regions of the specimens are inspected after the C-profiles completely separate. The photos, taken from both sides of the weld, are presented in Figure 19, where for each specimen the upper photo corresponds to the vertical profile, and the bottom photo to the horizontal profile. The images reveal that the welded regions are not of a rectangular shape, as numerically simulated and as seen from the imprint of the welding tooling on the outside in Figure 4, but rather an elliptical shape. Moreover, it can be seen that some fiber pullout occurred, more noticeable on specimens 1, 2, and 3.

4.3. Numerical – experimental comparison

The load-displacement curves obtained from the preliminary numerical simulations are compared to the curves measured during the tests and are presented in Figure 20, where dotted lines refer to the numerical simulations and continuous lines correspond to the experimental results.

The load-displacement responses show a clear difference between the numerical and experimental initial stiffness values, with the experimental values up to 35% lower than the

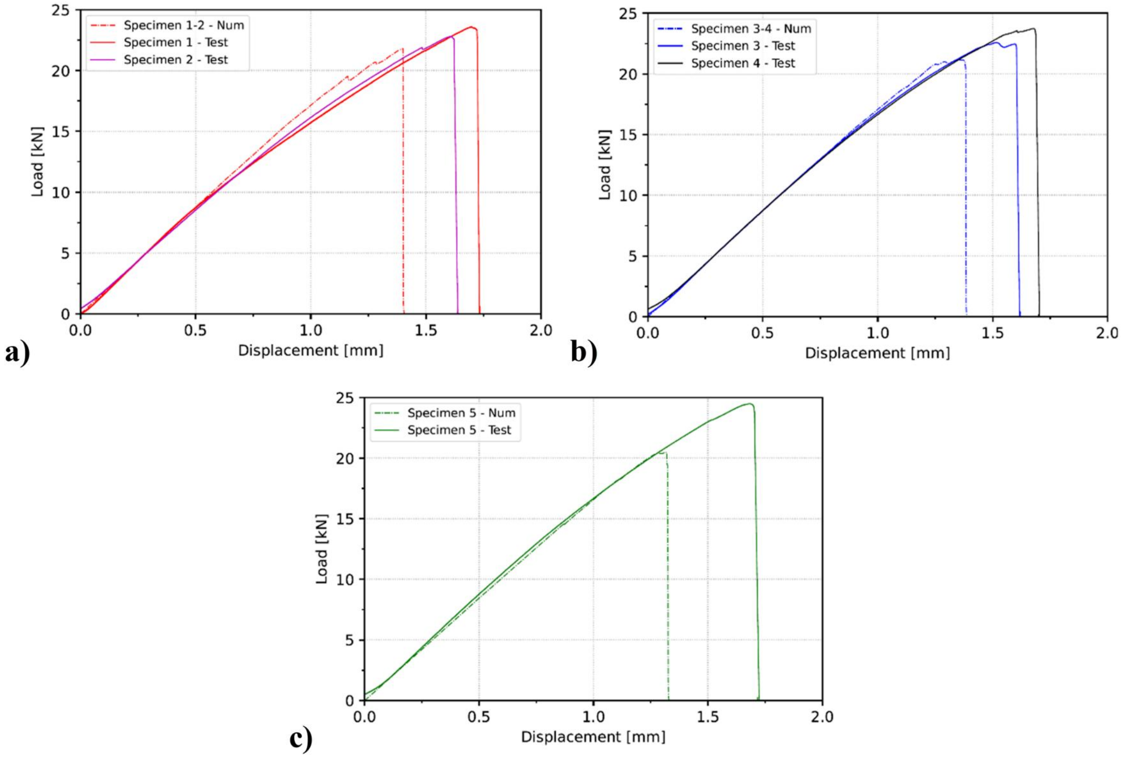

Figure 23. Numerical and experimental load-displacement curves for the specimens with the three welding configuration: (a) vertical; (b) horizontal; (c) horizontal (joined).

Table 7. Results from the updated numerical analyses for the three welding configurations.

Specimen	Welding configuration	Initial stiffness [kN/mm]	Maximum load [kN]	Displacement at maximum load [mm]
1–2	Vertical	17.4	21.7	1.41
3-4	Horizontal	17.2	21.2	1.38
5	Horizontal (joined)	16.9	20.7	1.33

numerical prediction. However, the maximum load is accurately predicted by the numerical simulations, as the difference between experimental and numerical values is between 3 and 9%.

Moreover, it is noticeable that the experimental results indicate specimen 5 as the best performing component, both in terms of initial stiffness and maximum load, while the simulations predict the opposite. This could be caused by a certain interference during the conduction welding process due to the fact that both welded strips are next to each other and some interaction between welds is expected. In the numerical model, the welding of specimen 5 is simulated as a single rectangular weld strip with double width.

A comparison of the out-of-plane displacements between the numerical model and the experimental results for each configuration is reported in Figure 21. It can be seen that, although there is a difference in the magnitude of the out-of-plane displacement values, which are about half in the numerical model respect to the experimental data, the deformed shape is accurately predicted with the upper flange of the horizontal profile moved toward the viewer.

5. Updated numerical model

From the comparison between the results of the preliminary numerical analyses and the experimental measured data, it is evident that, while the maximum load withstood by the test specimens is accurately predicted, the stiffness and consequently the displacement at the separation are significantly different. The main reason for this discrepancy is identified in the compliance of the support structure used in the experimental campaign. Indeed, in the preliminary numerical analyses, the support structure has been modeled as rigid, however, as it can be noted observing the horizontal displacements measured by the DIC during the experimental tests, shown in the first column of Figure 17, the horizontal profile rotates along the Z-axis. Using the values of the horizontal displacements measured at the four corners of the horizontal profile, a rotation of 0.57° is estimated. In order to verify this assumption, the numerical model is updated by modifying the boundary conditions. A rigid body is defined to constraint the motion of the nodes in the areas in contact with the support structure to the motion of two reference points. All the degree of freedoms of the reference points are blocked except for the rotation around the Z-axis, for which a maximum inward rotation of 0.57° is allowed. The updated boundary conditions are schematically represented in Figure 22.

The load-displacement curves resulting from the updated numerical model are compared with the experimental tests in Figure 23, with a summary of the most relevant updated numerical data reported in Table 7.

When comparing these results with those from the preliminary numerical simulations with the fully fixed boundary conditions shown in Table 5, it can be seen that the displacement at the separation is increased by around 50% when rotation is allowed, while maximum load values are reduced by 8% on average. However, the updated simulations match significantly better the experimental results, with almost identical initial stiffness values, and a discrepancy in the maximum load values between 6 and 15%.

The updated numerical analyses are able to well reproduce the experimental observed behavior before the welds begin to separate, especially for the horizontal welding configurations in Figures 23b and 23c. A slight discordance is seen for the case with the vertical welds (Figure 23a), with the stiffness of the updated numerical model being higher than the experimental one after a load of 10 kN.

Numerical and experimental results obtained in this work suggest that variations in welding configurations have minimal impact on the failure load for this particular component. The tested specimens demonstrate consistent structural behavior, with minor variations in the deformed shapes, and failure occurring suddenly with limited or no signs of propagation. The strength of the joint appears to be influenced by the total welded area, which remains consistent across all configurations, rather than by the orientation and positioning of the welding strips.

6. Conclusions

The behavior and performance of conduction welded specimens have been investigated considering three different welding configurations. The specimens are representative of the vertical C-struts which connect the frame to the passenger floor in the STUNNING thermoplastic fuselage. The investigated welded C-struts featured two welded strips of 60 by 19 mm. The nominal area of the welded regions is the same across all configurations, although the alignment varies between specimens: two specimens have vertical welded areas with a 13 mm gap between them, another two specimens have horizontal welded areas also 13 mm apart, and the last specimen presents the horizontal welded areas side by side. The specimens are subjected to vertical load to investigate the structural behavior and the strength of the welding.

Preliminary numerical analyses have been performed using finite element analysis in combination with the virtual crack-closure technique to simulate the failure of the welding. The results have shown minor differences in the performance in terms of stiffness and maximum load and displacement among the three different welding configurations.

From the numerical-experimental comparison, it has been observed that the stiffness obtained by the preliminary numerical analyses is up to 35% higher than the experimental tests. This discrepancy has been attributed to the compliance of the support structure, which was assumed rigid in the preliminary analyses. Therefore, an updated numerical model has been developed introducing appropriate boundary conditions to follow the deformations of the support structure observed during the tests. The updated numerical model has allowed to obtain better simulation with a maximum deviation in term of stiffness of 3.5%, although the difference in maximum load is between 6 and 15%.

Experimental tests indicate that the total welded area plays a predominant role in determining joint strength, with minimal differences observed across different orientations and placements of the welding strips. Additional research is required to explore how the ply orientation at the weld interface affects the failure load and to evaluate the energy-absorbing capabilities of thermoplastic welds under dynamic loading conditions. Overall, this research has contributed in providing valuable experimental and numerical insights to fully unlock the potential of thermoplastic welded joints in aeronautical applications.

Acknowledgments

The authors would like to thank GKN Fokker for the manufacturing of the test specimens used for this research.

Disclosure statement

The results, opinions, conclusions, etc. presented in this work are those of the authors only and do not necessarily represent the position of the JU; the JU is not responsible for any use made of the information contained herein. No potential conflict of interest was reported by the author(s).

Funding

This research has partially received funding from the Clean Sky 2 Joint Undertaking (JU) under grant agreement No 945583, STUNNING. The JU receives support from the European Union's Horizon 2020 research and innovation program and the Clean Sky 2 JU members other than the Union.

References

[1] F. Ozturk, M. Cobanoglu, and R.E. Ece, Recent advancements in thermoplastic composite materials in aerospace industry, J. Thermoplast. Compos., 2023. DOI: 10.1177/08927057231222820.

[2] G. Di Giorgio, Safety and accidents involving aircraft manufactured from polymer composite materials: a review, Aerotec. Missili Spaz., vol. 102, no. 4, pp. 337–353, 2023. DOI: 10.1007/s42496-023-00170-9.

[3] T.C. Silva, D.V.O. Moraes, G.F.M. Morgado, V.O. Gonçalves, D.H.S. Costa, T.P.Z. Marques, F.R. Passador, and M.C. Rezende, Mechanical characterization and fractographic study of the carbon/PEI composite under static and fatigue loading, Mech. Adv. Mater. Struc., vol. 31, no. 6, pp. 1291–1299, 2024. DOI: 10.1080/15376494.2022.2134952.

[4] A. Pegoretti, Towards sustainable structural composites: A review on the recycling of continuous-fiber-reinforced thermoplastics, Adv. Ind. Eng. Polym. Res., vol. 4, no. 2, pp. 105–115, 2021. DOI: 10.1016/j.aiepr.2021.03.001.

[5] J. Barroeta Robles, M. Dubé, P. Hubert, and A. Yousefpour, Repair of thermoplastic composites: an overview, Adv. Manuf. Polym. Compos. Sci., vol. 8, no. 2, pp. 68–96, 2022. DOI: 10.1080/20550340.2022.2057137.

[6] G.D. Goh, V. Dikshit, J. An, and W.Y. Yeong, Process-structure-property of additively manufactured continuous carbon

fiber reinforced thermoplastic: an investigation of mode I interlaminar fracture toughness, Mech. Adv. Mater. Struc., vol. 29, no. 10, pp. 1418–1430, 2022. DOI: 10.1080/15376494.2020.1821266.

[7] A. Siddique, Z. Iqbal, Y. Nawab, and K. Shaker, A review of joining techniques for thermoplastic composite materials, J. Thermoplast. Compos., vol. 36, no. 8, pp. 3417–3454, 2022. DOI: 10.1177/08927057221096662.

[8] F. Atzler, L. Raps, J. Freund, S. Tröger, and S. Hümbert, Bonding of low-melting polyaryletherketone onto polyamide 6: a concept for molds for automated fiber placement, J. Compos. Sci., vol. 7, no. 9, pp. 371, 2023. DOI: 10.3390/jcs7090371.

[9] D. Peeters, G. Clancy, V. Oliveri, R. O'Higgins, D. Jones, and P.M. Weaver, Concurrent design and manufacture of a thermoplastic composite stiffener, Compos. Struct., vol. 212, pp. 271–280, 2019. DOI: 10.1016/j.compstruct.2019.01.033.

[10] S.K. Bhudolia, G. Gohel, K.F. Leong, and A. Islam, Advances in ultrasonic welding of thermoplastic composites: a review, Materials., vol. 13, no. 6, pp. 1284, 2020. DOI: 10.3390/ma13061284.

[11] M. Russello, G. Catalanotti, S.C. Hawkins, and B.G. Falzon, Resistance welding of carbon fibre reinforced PEKK by means of CNT webs, J. Compos. Mater., vol. 57, no. 1, pp. 79–94, 2023. DOI: 10.1177/00219983221138952.

[12] D. Barazanchy, and M. van Tooren, Heating mechanisms in induction welding of thermoplastic composites, J. Thermoplast. Compos., vol. 36, no. 2, pp. 473–492, 2023. DOI: 10.1177/08927057211011621.

[13] J.W. van Ingen, Thermoplastic orthogrid fuselage shell, Sampe J., vol. 52, pp. 7–15, 2016.

[14] J.W. van Ingen, J. Waleson, A. Offringa, and M. Chapman, Double curved thermoplastic orthogrid rear fuselage shell, in SAMPE Europe Conference, Nantes, France, pp. 1–10, 2019.

[15] S.L. Omairey, S. Sampethai, L. Hans, C. Worrall, S. Lewis, D. Negro, T. Sattar, E. Ferrera, E. Blanco, J. Wighton, L. Muijs, S.L. Veldman, M. Doldersum, R. Tonnaer, N. Jayasree, and M. Kazilas, Development of innovative automated solutions for the assembly of multifunctional thermoplastic composite fuselage, Int. J. Adv. Manuf. Technol., vol. 117, no. 5–6, pp. 1721–1738, 2021. DOI: 10.1007/s00170-021-07829-2.

[16] S.L. Veldman, P. Kortbeek, P.C. Wölcken, R.H.J. Kos, and I.V. Fernandez, Development of a multifunctional fuselage demonstrator, Proceedings of Aerospace Europe Conference, Bordeaux, France, 2020.

[17] T. Zhao, G. Palardy, I.F. Villegas, C. Rans, M. Martinez, and R. Benedictus, Mechanical behaviour of thermoplastic composites spot-welded and mechanically fastened joints: a preliminary comparison, Compos. Part B-Eng., vol. 112, pp. 224–234, 2017. DOI: 10.1016/j.compositesb.2016.12.028.

[18] N. Azinan, A. Halim Kadarman, and J.S.S. Sidhu, An overview of fatigue models for composite laminate materials, Mech. Adv. Mater. Struc., vol. 29, no. 25, pp. 4389–4411, 2022. DOI: 10.1080/15376494.2021.1929591.

[19] J. Kupski, S. Teixeira de Freitas, D. Zarouchas, P.P. Camanho, R, and Benedictus, R., Composite layup effect on the failure mechanism of single lap bonded joints, Compos. Struct., vol. 217, pp. 14–26, 2019. DOI: 10.1016/j.compstruct.2019.02.093.

[20] B.H.A.H. Tijs, S. Abdel-Monsef, J. Renart, A. Turon, and C. Bisagni, Characterization and analysis of the interlaminar behavior of thermoplastic composites considering fiber bridging and R-curve effects, Compos. Part A-Appl S., vol. 162, pp. 107101, 2022. DOI: 10.1016/j.compositesa.2022.107101.

[21] K. van Dooren, B. Tijs, J. Waleson, and C. Bisagni, Skin-stringer separation in post-buckling of butt-joint stiffened thermoplastic composite panels, Compos. Struct., vol. 304, pp. 116294, 2023. DOI: 10.1016/j.compstruct.2022.116294.

[22] S. Wang, J. Zhang, Z. Zhou, G. Fang, and Y. Wang, Compressive and flexural behavior of carbon fiber-reinforced PPS composites at elevated temperature, Mech. Adv. Mater. Struc., vol. 27, no. 4, pp. 286–294, 2020. DOI: 10.1080/15376494.2018.1472334.

[23] S. Higuera, R. Miralbes, and D. Ranz, Mechanical properties and energy–absorption capabilities of thermoplastic sheet gyroid structures, Mech, Adv. Mater. Struc., vol. 29, no. 25, pp. 4110–4124, 2022. DOI: 10.1080/15376494.2021.1919803.

[24] A. Oktav, M.A. Başaran, and F. Darıcık, Dynamic response optimization of a thermoplastic composite sandwich beam under random vibration, Mech. Adv. Mater. Struc., pp. 1–14, 2023. DOI: 10.1080/15376494.2023.2227182.

[25] A.K. Ravi, A. Bhasin, L. Gomez, G. Olivares, and N. Kawamura, Experimental and numerical analysis of welded thermoplastic joints, (2023), In Proceedings of ASC – 38th Technical Conference, Boston, MA, USA, pp. 1606–1618, 2023.

[26] J. Kreikemeier, and A. Abdulkadir, Numerical analysis of thermoplastically welded CFRP structures, Appl. Compos. Mater., vol. 30, no. 1, pp. 73–91, 2023. DOI: 10.1007/s10443-022-10076-7.

[27] B.H.A.H. Tijs, M. Doldersum, A. Turon, J. Waleson, and C. Bisagni, Experimental and numerical evaluation of conduction welded thermoplastic composite joints, Compos. Struct., vol. 281, pp. 114964, 2022. DOI: 10.1016/j.compstruct.2021.114964.

[28] K. van Dooren, and C. Bisagni, Design, analysis and testing of thermoplastic welded stiffened panels to investigate skin-stringer separation in post-buckling, Compos. Part B-Eng., vol. 267, pp. 111033, 2023. DOI: 10.1016/j.compositesb.2023.111033.

[29] SAM XL, Smart Advanced ManufacturingXL, Delft University of Technology, Delft, The Netherlands. Available from: https://www.tudelft.nl/lr/samxl (accessed Mar 16, 2024).

[30] E. Clarkson, Medium Toughness PAEK Thermoplastics Toray (Formerly TenCate) Cetex® TC1225 (LM PAEK) T700GC 12K T1E Unidirectional Tape 145 Gsm 34% RC Material Allowables Statistical Analysis Report, Wichita State University NCAMP, Kansas, United States, 2021.

[31] RenCast© CW2418-1/HY5160-61-62 HY5118, Casting resin, metal filled, epoxy resin systems, Huntsman advanced materials, 2012. Available from https://www.generaladhesivos.com/proveedor-pegamento/904hoja-tecnica-CW%202418-1%20_%20HY%205160_%2061_62_%20HY%205118_eur_sp.pdf (accessed Mar 16, 2024).

[32] Abaqus Analysis Guide, Dassault Systemes: Vélizy-Villacoublay, France, 2021.

[33] M.L. Benzeggagh, and M. Kenane, Measurement of mixed-mode delamination fracture toughness of unidirectional glass/epoxy composites with mixed-mode bending apparatus, Compos. Sci. Technol., vol. 56, no. 4, pp. 439–449, 1996. DOI: 10.1016/0266-3538(96)00005-X.

[34] VIC 3D User Manual, Correlated Solutions, Columbia, South Carolina, United States, 2022.